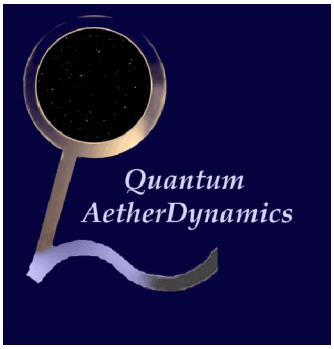

Quantum AetherDynamics Institute (QADI)

QMU Registration of Gyroscopic Coupling in a Nonspinning Ferromagnet

Public-Trace Reproduction, a Composition Envelope, and a Material-Participation Constraint

David W. Thomson III
Quantum AetherDynamics Institute (QADI), Alma, Illinois, USA
ORCID: 0000-0002-5830-5427

Working Manuscript v1.0 – August 9, 2026

This article is published by the Quantum AetherDynamics Institute (QADI).

It develops the Aether Physics Model (APM)

Abstract

Ahrens and Vinante recently measured gyroscopic spin–rotation coupling in a nonspinning, superconductively levitated ferromagnetic microsphere. We perform an independent reconstruction from their public archive and register the result in Quantum Measurement Units (QMU). All five deposited checksums are verified, and 315 raw two-channel traces are analyzed using the correlation model stated in the supplement. Three of four reconstructed Einstein–de Haas frequencies agree with the published central values within 0.3%; the remaining dataset is consistent within 1.24 combined standard deviations. The published material factors give the descriptive inverse-variance result $g = 1.16263 \pm 0.02578$, and therefore $\Gamma_{\mathrm{QMU}} \equiv (\mu\,\mathrm{ccf/magm})/(S/\mathrm{angm}) = g/2 = 0.58131 \pm 0.01289$. Using magm/angm = 1/mchg, we derive the exact collective identity $\Gamma_{\mathrm{QMU}} = (\mu\,\mathrm{ccf}/S)\mathrm{mchg}$ and its spherical-particle closure. Five public representations of the commercial MQP-S-11-9-20001 composition are then evaluated with the deliberately simplified constituent model used in the source article. Across the reported composition envelope, this control gives $g_{\mathrm{ctrl}} = 1.3647$–$1.3952$, above the measured value. Within that model, agreement requires a rare-earth share of modeled angular momentum near 0.661 instead of 0.478–0.501, equivalently a transition-metal participation factor of 0.468–0.516. These are quantitative material constraints rather than fitted APM predictions. The analysis establishes a reproducible QMU target for a future species- and phase-resolved calculation and identifies composition-, phase-, and temperature-series experiments capable of distinguishing competing closures.

Keywords: gyromagnetism; Einstein–de Haas effect; levitated ferromagnet; magnetic moment; angular momentum; QMU; Aether Physics Model; MQP-S-11-9; reproducibility

1 Introduction

The Einstein–de Haas relation connects magnetization to mechanical angular momentum. Ahrens and Vinante extended this relation to a particularly clean regime: a hard permanent ferromagnet that is not intentionally spinning, yet couples two orthogonal librational modes through its intrinsic angular momentum [Ahrens and Vinante, 2026]. The experiment is valuable for independent analysis because the coupling estimator is calibration-free and the authors deposited both processed measurements and raw two-channel traces [Ahrens and Vinante, 2025b].

The source article reports four determinations of the Einstein–de Haas frequency f_I and the collective gyromagnetic factor g. Its simplest constituent estimate, based on $Nd_2Fe_{14}B$, gives $g_{\mathrm{eff}} = 1.28$, whereas the measured values lie between 1.10 and 1.19. The microspheres, however, are made from a commercial Nd–Pr–Fe–Co–Ti–Zr–B powder rather than a single ideal phase.

This paper asks a narrower and reproducible question: what exactly does the experiment constrain when magnetic moment and angular momentum are registered in QMU? We maintain a strict separation between

1. deposited measurements;
2. independent reconstruction;
3. exact unit registration;
4. a conventional constituent control; and
5. an APM prediction that remains to be derived.

This separation prevents a QMU change of variables from being mistaken for new empirical support. The result is a dimensionless material-participation ratio $\Gamma_{\mathrm{QMU}} = g/2$ and a quantitative composition-envelope constraint. The latter defines what a species- and phase-resolved APM calculation must explain without fitting the observed coupling.

The institutional QMU definitions and paper archive follow the QADI reference identity [Thomson III, 2025a]. Experimental quantities are retained in their deposited units when reproducing the measurement; QMU provides the primary theoretical registration, with the explicit SI bridge collected in the derivation and appendices.

2 Experimental Target and Public Archive

2.1 Coupled rotational motion

For small angular displacements α and β, the source model is

$$\ddot{\alpha} + \omega_\alpha^2 \alpha + \omega_I \dot{\beta} = 0, \tag{1}$$

$$\ddot{\beta} + \omega_\beta^2 \beta - \omega_I \dot{\alpha} = 0, \tag{2}$$

where $\omega_I = S/I$, S is the intrinsic angular momentum rigidly attached to the magnet, and I is its moment of inertia. The gyroscopic term produces an out-of-phase secondary component in each predominantly librational mode.

For the quasi-α and quasi-β excitations, the fitted correlation quadratures define

$$r_\alpha = \frac{s_{12}^{(\alpha)}}{c_{11}^{(\alpha)}}, \qquad r_\beta = \frac{s_{21}^{(\beta)}}{c_{22}^{(\beta)}}. \tag{3}$$

The calibration-free estimator is

$$r_\alpha r_\beta = \frac{\omega_\alpha \omega_\beta}{(\omega_\beta^2 - \omega_\alpha^2)^2}\, \omega_I^2, \qquad f_I = \frac{\omega_I}{2\pi}. \tag{4}$$

The collective factor is inferred from

$$g = \frac{\mu/\mu_B}{S/\hbar}. \tag{5}$$

2.2 Archive integrity and inventory

The Zenodo record contains four processed-data files, a readme, and a compressed archive of the raw traces [Ahrens and Vinante, 2025b]. The MD5 value of every file matches the record. The compressed archive is 693,262,758 bytes, passes an integrity test, and contains 340 entries. Of these, 315 are CSV traces totaling 2,707,852,141 uncompressed bytes. The trace inventory is 128/64 α/β traces for Dataset 1, 15/15 for Dataset 2, 15/14 for Dataset 3, and 32/32 for Dataset 4.

The final article is used for the published results. The arXiv version is used for the appended numerical supplement [Ahrens and Vinante, 2025a]. The authors' analysis code was not deposited; the present implementation is therefore an independent reconstruction from the stated equations rather than a bitwise reproduction.

3 Independent Public-Trace Reconstruction

3.1 Numerical procedure

For each pair of raw channels, we compute the auto- and cross-correlations in Supplement Eq. S10. The primary reconstruction fits each correlation over three mode periods around zero delay to

$$C_{ij}(\tau) = A_0(1 - A_1|\tau|)\cos(2\pi f\tau + \phi), \tag{6}$$

with amplitude, envelope slope, mode frequency, and phase free. The fitted quadratures are $c_{ij} = A_0\cos\phi$ and $s_{ij} = -A_0\sin\phi$. A separate harmonic fit to the two time channels provides a diagnostic cross-check.

The raw channel polarity is not specified in the repository. Signed ratios are retained in the per-trace output; only the magnitude of the product of the two mean ratios enters equation (4). Uncertainty is propagated from the standard errors of the two ratio means, matching the supplement's stated procedure.

3.2 Reproduction results

Table 1: Published and independently reconstructed Einstein–de Haas frequencies. The combined z uses the quadrature sum of the two reported uncertainties.

Data	traces α/β	published f_I (Hz)	reconstructed f_I (Hz)	diff. (%)	z
D1	128/64	0.330 ± 0.040	0.3875 ± 0.0234	+17.417	+1.241
D2	15/15	0.620 ± 0.020	0.6197 ± 0.0216	-0.052	-0.011
D3	15/14	0.880 ± 0.050	0.8778 ± 0.0543	-0.250	-0.030
D4	32/32	0.860 ± 0.030	0.8575 ± 0.0303	-0.286	-0.058

Table 1 and figure 1 show that Datasets 2–4 reproduce to better than 0.3% in central value. Dataset 1 reconstructs 17.4% high but is consistent within 1.24 combined standard deviations. Its α quadrature ratio is only 1.77×10^{-5}, so detrending, lag-window, and envelope choices have disproportionate leverage. A harmonic cross-check gives the same qualitative result.

The processed tunability file provides an additional consistency check. The 17-point decreasing branch is linear in f_α^2, with $R^2 = 0.999925$. Its slope is -405.991 ± 0.908 Hz^2/mA, and its extrapolated zero is 11.1900 ± 0.0220 mA. The optical ellipticity file has median 0.689%, mean 0.926%, and maximum 4.73%; 15 of 22 entries are at or below 1%. The upper-tail value is retained as a shape-systematics caution.

4 QMU Registration

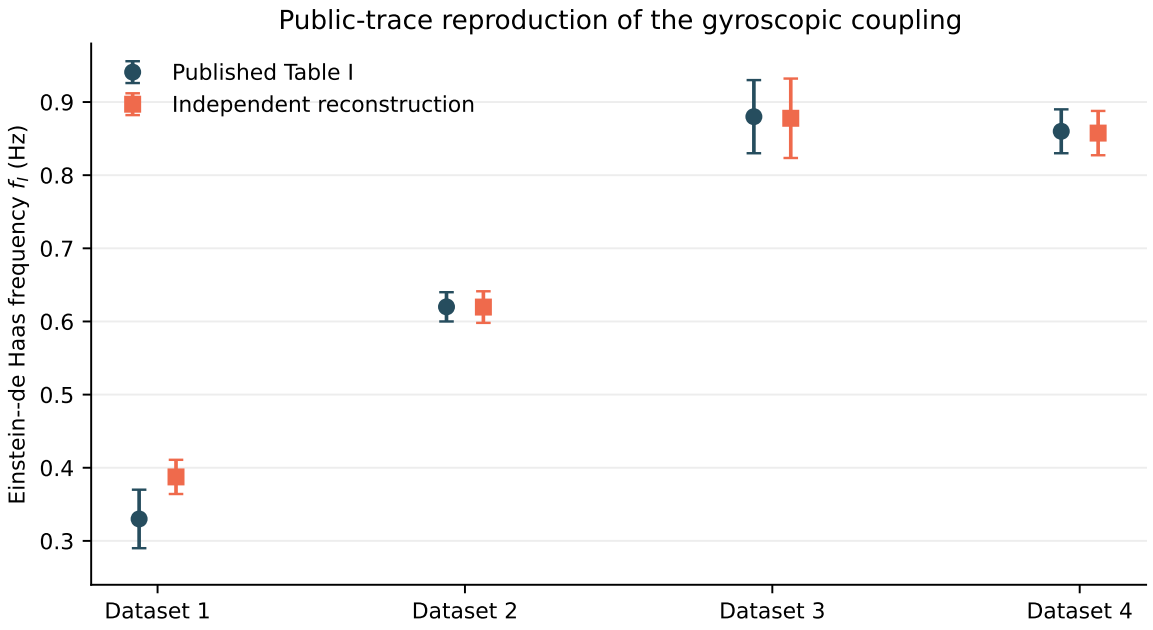

Figure 1: Public-trace reproduction of the central experimental observable. Error bars are the uncertainties reported in Table I of the source article and the standard errors propagated by the independent correlation reconstruction.

4.1 Base identities and exact bridge

The QMU angular-momentum and magnetic-moment units used here are [Thomson III, 2025b, 2026, Quantum AetherDynamics Institute, 2026]

$$\mathrm{angm} = h = m_{\mathrm{e}} {\lambda_C}^2 F_q, \qquad \mathrm{magm} = {e_{\mathrm{emax}}}^2 {\lambda_C}^2 F_q. \tag{7}$$

The corresponding conversion and ratio units are

$$\mathrm{ccf} = \frac{{e_{\mathrm{emax}}}^2}{e}, \qquad \mathrm{mchg} = \frac{m_{\mathrm{e}}}{{e_{\mathrm{emax}}}^2}, \qquad \mathrm{volm} = {\lambda_C}^3. \tag{8}$$

Two correlations follow immediately:

$$\boxed{\frac{\mathrm{magm}}{\mathrm{angm}} = \frac{1}{\mathrm{mchg}}}, \qquad \boxed{\mathrm{ccf}\,\mathrm{mchg} = \frac{m_{\mathrm{e}}}{e}}. \tag{9}$$

The first relation shows that the magnetic-moment-to-angular-momentum unit ratio is the reciprocal of mchg. The second is the exact bridge connecting the QMU distributed magnetic-charge conversion to the familiar electron mass-to-charge ratio.

The Bohr bridge is not an independent assumption. From $\mu_B = e\hbar/(2m_{\mathrm{e}})$, $\hbar = h/(2\pi)$, and $h = \mathrm{angm}$,

$$\mu_B \mathrm{ccf} = \frac{e\hbar}{2m_{\mathrm{e}}} \frac{{e_{\mathrm{emax}}}^2}{e} = \frac{\mathrm{magm}}{4\pi}. \tag{10}$$

Define the registered collective quantities

$$q_\mu \equiv \frac{\mu\,\mathrm{ccf}}{\mathrm{magm}}, \qquad q_S \equiv \frac{S}{\mathrm{angm}}. \tag{11}$$

Substitution of equations (5) and (10) gives the exact dimensionless ratio

$$\boxed{\Gamma_{\mathrm{QMU}} \equiv \frac{q_\mu}{q_S} = \frac{g}{2} = \left(\frac{\mu\,\mathrm{ccf}}{S}\right)\mathrm{mchg}.} \tag{12}$$

Equation (12) registers the measured gyromagnetic relation in QMU. By itself it is algebraically equivalent to equation (5); it becomes predictive only when q_μ and q_S are independently calculated from material structure.

4.2 Spherical-particle closure

For a sphere of magnetization M, density ρ, volume V, and radius R,

$$\mu = MV, \qquad I = \frac{2}{5}\rho V R^2, \qquad S = 2\pi I f_I. \tag{13}$$

The volume cancels in equation (12), producing

$$\boxed{\Gamma_{\mathrm{QMU}} = \frac{5M\,\mathrm{ccf}\,\mathrm{mchg}}{4\pi\rho R^2 f_I} = \frac{5M m_{\mathrm{e}}}{4\pi\rho R^2 f_I e}.} \tag{14}$$

The second equality is the exact SI bridge of $\mathrm{ccf}\,\mathrm{mchg} = m_{\mathrm{e}}/e$; it contains no fitted conversion coefficient.

A QMU-only dimensionless form is obtained with

$$\widehat{M} = \frac{M\mathrm{ccf}}{\mathrm{magm/volm}}, \quad \widehat{\rho} = \frac{\rho}{m_{\mathrm{e}}/\mathrm{volm}}, \quad \widehat{R} = \frac{R}{\lambda_C}, \quad \widehat{f_I} = \frac{f_I}{F_q}. \tag{15}$$

Then

$$\boxed{\widehat{f_I} = \frac{5}{4\pi\Gamma_{\mathrm{QMU}}}\frac{\widehat{M}}{\widehat{\rho}\,\widehat{R}^2}.} \tag{16}$$

This closure expresses the measured mechanical response entirely as a ratio of QMU quantities: magnetic-moment density, mass density, particle size, and the material participation factor.

4.3 Registered experimental values

Table 2: QMU registration from the rounded R, M, and f_I values in the source Table I. The final two columns obey $g = 2\Gamma_{\mathrm{QMU}}$.

Data	q_μ	q_S	Γ_{QMU}	g
1	6.45153×10^{14}	1.15172×10^{15}	0.56016	1.12033
2	3.18897×10^{14}	5.35813×10^{14}	0.59517	1.19033
3	1.41509×10^{14}	2.57224×10^{14}	0.55014	1.10028
4	1.38759×10^{14}	2.38423×10^{14}	0.58199	1.16397

Using the authors' tabulated g values rather than recomputing from rounded inputs, the descriptive inverse-variance fit is

$$g_{\mathrm{mat}} = 1.16263 \pm 0.02578, \qquad \Gamma_{\mathrm{mat}} = 0.58131 \pm 0.01289, \tag{17}$$

with $\chi^2 = 1.414$ for three degrees of freedom ($p = 0.702$). This uncertainty assumes the four tabulated errors are independent. The supplement identifies a 5% density-scale uncertainty, and Datasets 3 and 4 use the same particle. The covariance matrix is not deposited. As a sensitivity case, adding a fully shared 5% scale in quadrature expands the uncertainties to 0.06359 for g and 0.03179 for Γ; this is not asserted as an additional known error.

The invariant $f_I R^2/M$ is consistent across the four configurations: $\chi^2 = 0.969$ for three degrees of freedom ($p = 0.809$), using the published marginal uncertainties and neglecting unavailable covariance. Thus the public data show no resolved size- or cooldown-dependent correction to a common material factor (figure 2).

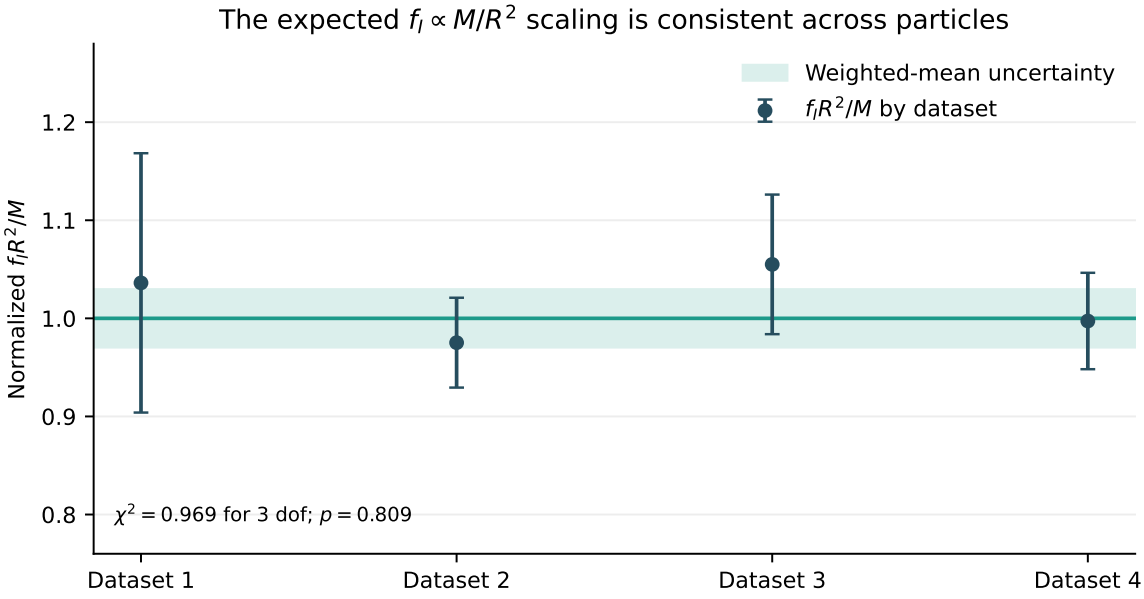

Figure 2: Normalized size-scaling invariant. The band is the uncertainty of the weighted mean under the stated independence approximation.

5 Public Composition Envelope

5.1 Composition evidence

The microspheres are identified as Magnequench MQP-S-11-9-20001 [Ahrens and Vinante, 2026, Magnequench, n.d.]. Independent studies identify the same commercial grade as a Nd-lean, multi-phase or nanocomposite Nd–Pr–Fe–Co–Ti–Zr–B powder and report closely related, but not identical, compositions [Yao et al., 2024, Pelevin et al., 2023, Wu et al., 2023]. Yao et al. identify $Nd_2Fe_{14}B$, $Nd_2Fe_{17}B_x$, α-Fe, Nd oxide, and a Zr/Ti/B-rich phase in related processing states; the starting

powder itself shows the expected $Nd_2Fe_{14}B/\alpha$-Fe nanocomposite character. No published chemistry is specific to the three levitated particles.

Four weight-percent reports were converted to atomic percent with IUPAC atomic weights [Prohaska et al., 2022]. The nominal atomic representation is included as a fifth consistency row.

Table 3: Public composition representations converted to atomic percent. Rows may reflect different lots and measurement methods; they define a sensitivity envelope rather than a sample certificate.

Source	Nd	Pr	Fe	Co	Ti	Zr	B
Supplier	7.520	0.723	75.337	2.542	2.379	2.628	8.871
Yao ICP	7.264	0.754	74.588	2.750	2.195	2.675	9.775
Pelevin	6.719	0.769	70.030	2.805	2.501	2.937	14.239
Wu	8.020	0.599	74.119	2.556	2.392	2.840	9.475
Nominal atomic	7.500	0.700	75.400	2.500	2.500	2.600	8.800

5.2 Deliberately simplified constituent control

To reproduce and extend the source article's control, assign

$$(g_{\mathrm{Nd}}, J_{\mathrm{Nd}}) = (8/11, 9/2), \quad (g_{\mathrm{Pr}}, J_{\mathrm{Pr}}) = (4/5, 4), \quad (g_{\mathrm{Fe}}, J_{\mathrm{Fe}}) = (2, 1/2). \tag{18}$$

Co is treated as an Fe-site spin-only replacement with $(g, J) = (2, 1/2)$; Ti, Zr, and B are inactive in this control. These assignments are intentionally simple. They are not a detailed band-structure or phase calculation.

For atom fractions x_i and J_i expressed in units of $\hbar$, the QMU population sums are

$$q_S^{\mathrm{ctrl}} = \frac{1}{2\pi} \sum_i x_i J_i, \qquad q_\mu^{\mathrm{ctrl}} = \frac{1}{4\pi} \sum_i x_i g_i J_i, \tag{19}$$

so that

$$\Gamma_{\mathrm{ctrl}} = \frac{q_\mu^{\mathrm{ctrl}}}{q_S^{\mathrm{ctrl}}} = \frac{g_{\mathrm{ctrl}}}{2}, \qquad g_{\mathrm{ctrl}} = \frac{\sum_i x_i g_i J_i}{\sum_i x_i J_i}. \tag{20}$$

The stoichiometric checks are $g_{\mathrm{ctrl}} = 1.28409$ for $Nd_2Fe_{14}B$ and 1.36000 for $Pr_2Fe_{14}B$, reproducing the source article to rounding.

5.3 Control values

The five representations give $g_{\mathrm{ctrl}} = 1.3647$–$1.3952$ and $\Gamma_{\mathrm{ctrl}} = 0.6823$–$0.6976$ (table 4 and figure 3). An element-wise sensitivity calculation samples uniformly between the extrema of the four public weight-percent reports and renormalizes each draw. For 200,000 deterministic-seed draws, its central 95% interval is $g_{\mathrm{ctrl}} = 1.3649$–$1.4019$. This interval describes sensitivity to the published composition range; it is not a manufacturing probability interval.

Table 4: Simplified constituent controls and the participation diagnostics required to equal the measured g. The quantity f_{RE} is the rare-earth share of modeled angular momentum; κ_{RE} scales the RE sector relative to the nominal model, and $\beta_{\mathrm{TM}} = 1/\kappa_{\mathrm{RE}}$ is the equivalent TM participation factor.

Source	g_{ctrl}	Γ_{ctrl}	$f_{\mathrm{RE,nom}}$	$f_{\mathrm{RE,req}}$	κ_{RE}	β_{TM}
Supplier	1.3850	0.6925	0.4854	0.6609	2.066	0.484
Yao ICP	1.3920	0.6960	0.4801	0.6611	2.113	0.473
Pelevin	1.3952	0.6976	0.4777	0.6614	2.136	0.468
Wu	1.3647	0.6823	0.5010	0.6603	1.936	0.516
Nominal atomic	1.3866	0.6933	0.4841	0.6608	2.076	0.482

The rare-earth-lean composition increases the simplified control relative to ideal $Nd_2Fe_{14}B$ because it shifts modeled angular momentum toward the $g = 2$ transition-metal sector. Any additional α-Fe fraction moves the same control upward. Thus composition and α-Fe, by themselves, do not lower this simplified estimate toward the observation.

5.4 Participation constraint

Separate the control sums into rare-earth (RE) and transition-metal (TM) contributions,

$$A_s = \sum_{i \in s} x_i J_i, \qquad B_s = \sum_{i \in s} x_i g_i J_i. \tag{21}$$

If κ_{RE} multiplies both RE moment and angular-momentum weights relative to TM, then

$$g(\kappa_{\mathrm{RE}}) = \frac{\kappa_{\mathrm{RE}} B_{\mathrm{RE}} + B_{\mathrm{TM}}}{\kappa_{\mathrm{RE}} A_{\mathrm{RE}} + A_{\mathrm{TM}}}, \tag{22}$$

and the value required by the experiment is

$$\kappa_{\mathrm{RE}} = \frac{B_{\mathrm{TM}} - g_{\mathrm{mat}} A_{\mathrm{TM}}}{g_{\mathrm{mat}} A_{\mathrm{RE}} - B_{\mathrm{RE}}}, \qquad \beta_{\mathrm{TM}} = \kappa_{\mathrm{RE}}^{-1}. \tag{23}$$

Across the public rows, $\kappa_{\mathrm{RE}} = 1.936$–$2.136$ and $\beta_{\mathrm{TM}} = 0.468$–$0.516$. The modeled RE share would have to rise from 0.478–0.501 to approximately 0.661. For the nominal atomic composition, $g_{\mathrm{ctrl}} = 1.38656$, $\Gamma_{\mathrm{ctrl}} = 0.69328$, $\kappa_{\mathrm{RE}} = 2.076$, and $\beta_{\mathrm{TM}} = 0.482$.

Equivalent one-number descriptions are a magnetic-participation deficit

$$D_\mu = 1 - \frac{\Gamma_{\mathrm{mat}}}{\Gamma_{\mathrm{ctrl}}} = 0.1615 \tag{24}$$

or, at fixed magnetic moment, an angular-participation surplus

$$D_S = \frac{\Gamma_{\mathrm{ctrl}}}{\Gamma_{\mathrm{mat}}} - 1 = 0.1926 \tag{25}$$

for the nominal atomic row. These alternatives are mathematically equivalent diagnostics; the present data do not identify which microscopic sector changes.

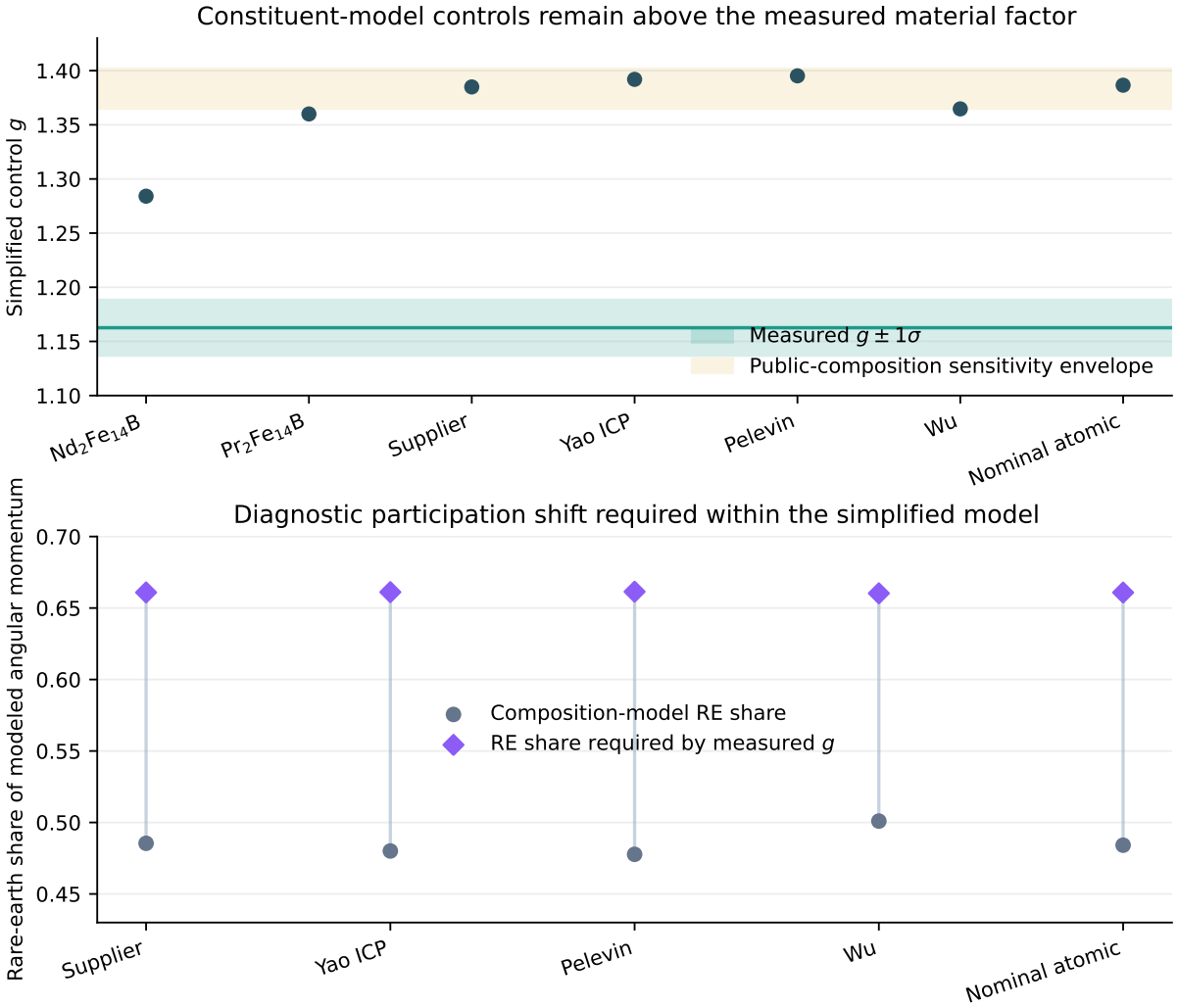

Figure 3: Top: simplified constituent controls compared with the measured material factor; the yellow band is the central 95% public-composition sensitivity envelope. Bottom: the rare-earth angular-momentum share present in each composition control and the share required to match the measured g.

6 Requirement for an APM Prediction

The exact registration in equation (12) does not predict the measured value. A genuine APM calculation must supply, before comparison,

$$\Gamma_{\mathrm{APM}} = \frac{\sum_{i,k} N_i p_{ik} q^{\mathrm{geom}}_{\mu,ik}}{\sum_{i,k} N_i p_{ik} q^{\mathrm{geom}}_{S,ik}}, \tag{26}$$

where i labels species, k labels magnetic phases, N_i is the species population, p_{ik} is an independently determined phase/participation fraction, and the QMU moments $q^{\mathrm{geom}}_{\mu,ik}$ and $q^{\mathrm{geom}}_{S,ik}$ follow from the species geometry. Importing measured atomic magnetic moments or adjusting p_{ik} to reproduce f_I would turn equation (26) into a retrodiction.

The measured target for such a calculation is equation (17). A conservative comparison should additionally repeat the test with the shared-scale sensitivity uncertainty. The public composition envelope supplies the prior range when the exact particle lot is unavailable.

The present calculation therefore makes two advances without claiming a completed APM test:

1. it identifies the exact QMU observable that an atomic model must predict; and
2. it quantifies how far the source article's simplified composition model must move in angular-momentum participation to reach that observable.

The experimentally registered QMU correlations can be summarized as

$$\frac{\mathrm{magm}}{\mathrm{angm}} = \frac{1}{\mathrm{mchg}}, \qquad \mu_B \mathrm{ccf} = \frac{\mathrm{magm}}{4\pi}, \qquad \Gamma_{\mathrm{QMU}} = \left(\frac{\mu\,\mathrm{ccf}}{S}\right)\mathrm{mchg}. \tag{27}$$

These relations isolate mchg as the QMU bridge between magnetic moment and angular momentum. A species-resolved prediction of the two population sums in equation (26) is therefore the shortest path from the measured gyroscopic coupling to an independently testable APM result.

7 Discriminating Experiments

The strongest next measurements are not additional repetitions at one composition. They are controlled changes that move the competing material closures in different directions.

1. **Composition series.** Repeat the spin–rotation measurement on powders spanning Nd/Pr ratio and rare-earth content. Report the observable directly as Γ_{QMU} through equation (14). The slope $\partial\Gamma_{\mathrm{QMU}}/\partial x_{\mathrm{RE}}$ tests species weights more strongly than a single absolute value.
2. **Phase series at fixed bulk chemistry.** Use thermal processing to vary $Nd_2Fe_{14}B$, α-Fe, and metastable phase fractions while holding elemental composition approximately fixed. The sign and magnitude of $\partial\Gamma_{\mathrm{QMU}}/\partial p_k$ directly test the participation factors in equation (26).
3. **Temperature sweep of one microsphere.** Follow f_I, M, and Γ_{QMU} through the low-temperature spin-reorientation region. A same-particle trajectory suppresses composition uncertainty and can separate a change in moment orientation from a change in total intrinsic angular momentum.

4. **Independent particle metrology.** Determine radius and shape by high-resolution imaging, density or mass independently of the trap model, and magnetic moment through a separate calibration. This breaks the covariance among R, M, and ρ that is unavailable in the current public record.
5. **Blind APM registration.** Freeze a species/phase ledger and its Γ_{APM} before opening the gyroscopic results for a new powder lot. This is the cleanest test against composition-dependent conventional controls.

The temperature series is especially efficient because the same particle can serve as its own composition and geometry control. The composition and phase series are more decisive for separating rare-earth and transition-metal weights. Together they convert the single measured value into derivatives with respect to independently controlled material variables.

8 Limitations

The correlation analysis follows the deposited equations, but analysis-code choices cannot be matched exactly because the original software is unavailable. Dataset 1 demonstrates the resulting sensitivity at very small quadrature.

The material mean treats four tabulated g uncertainties as independent even though two rows describe the same particle and some apparatus and material scales are shared. We therefore report both the descriptive uncertainty and a 5% shared-scale sensitivity case.

The composition rows are grade-level evidence from different lots and methods, not measurements of the levitated microspheres. The constituent control is the source article's intentionally simple ionic/spin model, extended to Co. It does not include crystal fields, noncollinear sublattices, orbital quenching, temperature-dependent exchange, or a measured phase inventory. Consequently, the separation between g_{ctrl} and g_{mat} is a motivation and a quantitative constraint, not a formal statistical rejection of materials theory.

Finally, the QMU identity $\Gamma_{\mathrm{QMU}} = g/2$ is an exact registration of the same observable. Independent empirical content enters only through a prior APM calculation of the numerator and denominator in equation (26).

9 Conclusions

The public data support the central observation of gyroscopic coupling in a nonspinning levitated ferromagnet. An independent analysis of all 315 raw traces reproduces three of four Einstein–de Haas frequencies within 0.3% and the fourth within 1.24 combined standard deviations.

QMU registration yields the exact material ratio

$$\Gamma_{\mathrm{QMU}} = \frac{\mu\,\mathrm{ccf/magm}}{S/\mathrm{angm}} = \left(\frac{\mu\,\mathrm{ccf}}{S}\right)\mathrm{mchg} = \frac{g}{2}, \tag{28}$$

with descriptive experimental target 0.58131 ± 0.01289. The associated spherical closure, equation (14), exposes the exact correlation $\mathrm{ccf}\,\mathrm{mchg} = m_{\mathrm{e}}/e$ and provides a direct experimental route to the QMU ratio.

The source article's simplified constituent control gives $g_{\mathrm{ctrl}} = 1.3647$–$1.3952$ across public compositions of the commercial grade. Within that model the experiment requires approximately half of the nominal transition-metal participation, or an equivalent increase of the rare-earth angular-momentum share to about 0.661. This is the principal new constraint of the reanalysis.

The work does not complete an APM prediction. It defines the number that must be predicted, the public composition range over which the prediction must remain stable, and the controlled experiments that can distinguish species- and phase-dependent closures. Those conditions make the levitated-ferromagnet platform a high-value target for a reproducible QADI research program.

Data and Code Availability

All experimental data are public at Zenodo record 17672632 [Ahrens and Vinante, 2025b]. This Overleaf project contains the paper source, figure-regeneration code, figure files, machine-readable result summaries, composition inputs, the claims ledger, and the package-validation report. The 661 MiB raw archive and the 2.7 GB expanded traces are not duplicated; they can be restored from Zenodo and verified by MD5. The deposited archive does not include the source authors' fitting code, so exact software-level replication of their pipeline is not claimed.

A QMU-to-SI Bridge and Uncertainty Details

A.1 Exact bridge chain

The SI comparison uses the current CODATA constants [Tiesinga et al., 2023]. The bridge begins with

$$h = \mathrm{angm} = m_{\mathrm{e}} {\lambda_C}^2 F_q, \qquad \mathrm{magm} = {e_{\mathrm{emax}}}^2 {\lambda_C}^2 F_q, \tag{29}$$

and therefore

$$\frac{\mathrm{magm}}{\mathrm{angm}} = \frac{{e_{\mathrm{emax}}}^2}{m_{\mathrm{e}}} = \frac{1}{\mathrm{mchg}}. \tag{30}$$

Multiplication of the Bohr magneton by the charge conversion factor gives

$$\mu_B \mathrm{ccf} = \frac{e\hbar}{2m_{\mathrm{e}}} \frac{{e_{\mathrm{emax}}}^2}{e} \tag{31}$$

$$= \frac{h {e_{\mathrm{emax}}}^2}{4\pi m_{\mathrm{e}}} \tag{32}$$

$$= \frac{\mathrm{magm}}{4\pi}. \tag{33}$$

Thus the conventional factor g and the QMU participation ratio satisfy

$$g = \frac{\mu/\mu_B}{S/\hbar} = 2\frac{\mu\,\mathrm{ccf}/\mathrm{magm}}{S/\mathrm{angm}} = 2\Gamma_{\mathrm{QMU}}. \tag{34}$$

For the spherical particle,

$$\Gamma_{\mathrm{QMU}} = \frac{5M}{4\pi\rho R^2 f_I}\,(\mathrm{ccf}\,\mathrm{mchg}) = \frac{5M m_{\mathrm{e}}}{4\pi\rho R^2 f_I e}. \tag{35}$$

The agreement between the two forms is limited only by numerical rounding of the bridge constants; the largest relative difference across the four rows is 4.11×10^{-12}.

A.2 Uncertainty propagation

For the reconstructed f_I, frequency uncertainty is negligible compared with the ratio uncertainty. With $f_I \propto (r_\alpha r_\beta)^{1/2}$,

$$\left(\frac{\sigma_{f_I}}{f_I}\right)^2 = \frac{1}{4}\left[\left(\frac{\sigma_{r_\alpha}}{r_\alpha}\right)^2 + \left(\frac{\sigma_{r_\beta}}{r_\beta}\right)^2\right]. \tag{36}$$

The combined z in table 1 is

$$z = \frac{f_{I,\mathrm{rec}} - f_{I,\mathrm{pub}}}{\sqrt{\sigma_{\mathrm{rec}}^2 + \sigma_{\mathrm{pub}}^2}}. \tag{37}$$

For direct use of equation (14) with independent inputs,

$$\left(\frac{\sigma_\Gamma}{\Gamma}\right)^2 = \left(\frac{\sigma_M}{M}\right)^2 + 4\left(\frac{\sigma_R}{R}\right)^2 + \left(\frac{\sigma_{f_I}}{f_I}\right)^2 + \left(\frac{\sigma_\rho}{\rho}\right)^2. \tag{38}$$

The source analysis infers R and M jointly from mechanical modes, so this independent-input expression is not used to replace the published g errors. A covariance-aware reanalysis requires the joint posterior or original fitting code.

B Reproducibility Inventory

The verified Zenodo files and MD5 values are listed in table 5. The raw archive passes `unzip -t`; its 315 CSV traces total 2,707,852,141 bytes when uncompressed.

Table 5: Verified public-data checksums.

File	Bytes	MD5
`readme.txt`	832	`cfddb87279baec59c83dffef4cd95038`
`Fig4_alpha_tunability.csv`	710	`d91b540799e0ebe9471d4598818ebfd5`
`FigS1_ellipticity.csv`	1,317	`94324d1bcb95c68591085a7896d73e03`
`FigS3_spectra.tsv`	624,547	`e7d6750a562191e9b6e29dabca7a6b5d`
`raw_traces_before_correlation.zip`	693,262,758	`b12c6c2937e0a770622ea9dc47ee0294`

The Overleaf package regenerates its figures and validates its machine-readable results from the project root:

```
python analysis/make_figures.py
latexmk -pdf main.tex
python analysis/validate_overleaf_project.py --pdf main.pdf
```

The machine-readable validation report records eight gate groups: deliverable inventory, five Zenodo checksum records, four-dataset reconstruction tolerances, processed-data controls, the material g fit

and QMU bridge closure, composition bounds, source cross-references, and PDF integrity. This is an internal-consistency test of the paper package. It does not rerun the 2.7 GB expanded raw-trace archive, and it does not convert the constituent control into an independent APM prediction.

Acknowledgments

The author thanks Felix Ahrens and Andrea Vinante for making the experimental data publicly available. No endorsement of the present interpretation by the source authors is implied. The Quantum AetherDynamics Institute is a U.S. 501(c)(3) public charity and independent nonprofit research organization developing the Aether Physics Model and Quantum Measurement Units [Thomson III, 2025a].

References

Felix Ahrens and Andrea Vinante. Observation of gyroscopic coupling in a non-spinning levitated ferromagnet, 2025a. URL https://arxiv.org/abs/2504.13744.

Felix Ahrens and Andrea Vinante. Dataset of paper "observation of gyroscopic coupling in a non-spinning levitated ferromagnet", 2025b.

Felix Ahrens and Andrea Vinante. Observation of gyroscopic coupling in a nonspinning levitated ferromagnet. *Physical Review Letters*, 136:146703, 2026. doi: 10.1103/hdh6-r1gy.

Magnequench. MQP-S-11-9-20001 isotropic powder. Product information, n.d. URL https://mqitechnology.com/product/mqp-s-11-9-20001/. Accessed 2026-08-09.

Ivan A. Pelevin et al. New scanning strategy approach for laser powder bed fusion of Nd–Fe–B hard magnetic material. *Metals*, 13(6):1084, 2023. doi: 10.3390/met13061084.

Thomas Prohaska, Johanna Irrgeher, Jacqueline Benefield, et al. Standard atomic weights of the elements 2021 (IUPAC technical report). *Pure and Applied Chemistry*, 94(5):573–600, 2022. doi: 10.1515/pac-2019-0603.

Quantum AetherDynamics Institute. QMU authority: Magnetic moment (magm), 2026. URL https://quantumaetherdynamics.org/qmu/magm.php. Accessed 2026-08-09.

David W. Thomson III. Quantum aetherdynamics institute (qadi): Community doi overview and citation guide. Zenodo, 2025a. URL https://doi.org/10.5281/zenodo.17479314.

David W. Thomson III. The charge conversion factor in the aether physics model: From singular to distributed charge, with rules, exceptions, and benchmarks, October 2025b. URL https://doi.org/10.5281/zenodo.17451188.

David W. Thomson III. Magnetic moment revisited: A quantum measurement unit analysis of particle magnetic moments and the neutron magnetic charge prediction, 2026. URL https://quantumaetherdynamics.org/papers/Neutron_Magnetic_Moment.pdf.

E. Tiesinga, P. J. Mohr, D. B. Newell, and B. N. Taylor. Codata recommended values of the fundamental physical constants: 2022. *Reviews of Modern Physics*, 95:025010, 2023. doi: 10.1103/RevModPhys.95.025010.

Julan Wu, Nesma T. Aboulkhair, Stuart Robertson, et al. Amorphous–crystalline nanostructured Nd–Fe–B permanent magnets using laser powder bed fusion: Metallurgy and magnetic properties. *Acta Materialia*, 259:119239, 2023. doi: 10.1016/j.actamat.2023.119239.

Bo Yao, Nan Kang, Xiangyu Li, and Xin Lin. Toward understanding the microstructure characteristics, phase selection and magnetic properties of laser additive manufactured Nd–Fe–B permanent magnets. *International Journal of Extreme Manufacturing*, 6:015002, 2024. doi: 10.1088/2631-7990/ad0472.